

Cycle-slip Detection and Repair Using a Low Cost Single Frequency Receiver with Inertial-aiding

Yu WANG, Signav, Telecom, ENAC, CAUC
Olivier JULIEN, Signav, Telecom, ENAC
Email: wang@recherche.enac.fr

BIOGRAPHIES

Yu Wang is a PhD candidate within the SIGNAL processing and NAVigation (SIGNAV) research group of the TELECOM laboratory inside the Ecole Nationale de l'Aviation Civile (ENAC), in Toulouse, France. Her study is funded by the Civil Aviation University of China (CAUC). She received in 2014 her engineering degree in digital communications from ENAC.

Olivier Julien is the head of SIGNAV research group of the TELECOM laboratory of ENAC, Toulouse, France. He received his engineering degree in 2001 in digital communications from ENAC and his PhD in 2005 from the Department of Geomatics Engineering of the University of Calgary, Canada. His research interests are turned towards the use of satellite-based navigation systems for safe navigation.

ABSTRACT

The general objective of this paper is to investigate the navigation performance one can expect from a low-cost architecture (single-frequency receiver with low-cost IMU) using carrier phase measurements in an urban canyon, where the frequency of occurrence of strong multipath environment, masking, *Non-Line-of-Sight* (NLOS) signal tracking, interference, etc.... is quite high and hard to mitigate.

On the GNSS side, a multi-constellation *Real-Time-Kinematic* (RTK) methodology is developed to take good care of frequent measurement losses and carrier-phase cycle slips. Then to take advantage of the complementary advantages of GNSS and INS, a closed-loop tightly coupled GNSS/INS structure with a low-cost *Micro Electro-Mechanical Systems* (MEMS) is applied to enhance the performance.

The proposed algorithm is finally tested based on data collected on the Toulouse semi-urban area as well as Toulouse city center.

1 INTRODUCTION

Until recently, to satisfy a centimeter-accuracy-demanding application, one or multiple high-precision GNSS receivers are used, and a tactical- or aviation-grade IMU can even be

integrated, which all cost much more than mass market can expect.

To achieve a precise positioning, carrier phase GNSS measurements should be used. The tracking errors associated to these measurements are significantly lower than those of code pseudo-ranges, but they suffer from two main drawbacks:

- The presence of an unknown integer number of carrier phase cycles called *ambiguity* prevents carrier phase measurements from acting as absolute pseudo-range measurements. The process to fix these ambiguities to their correct values is very sophisticated, and can be quite weak in adverse reception conditions, e.g. an urban canyon.
- The lack of robustness of these measurements resulting in frequent measurement losses and cycle slips (CS), especially in urban areas, which complicates the process to resolve for the carrier phase ambiguities.

As a consequence, until recently carrier phase measurements were used by applications that were taking place mostly in a benign open-space environment. For instance, the carrier-phase-involved RTK methodology has been widely approved to achieve precise positioning [20].

However, recent developments have enabled significant research efforts in this field for low-cost platforms. Most notably,

- Low-cost GNSS (and inertial) sensors and even cell-phone chips are now providing their raw measurements, including carrier phase measurements;
- There is now access to multiple GNSS constellations that allows a better selection of good measurements, even in degraded environments.

Recent work has thus started investigating the use of carrier phase measurements in urban and sub-urban areas.

Another common mean to improve positioning is the integration of INS, as the benefits and drawbacks of INS and GNSS are mostly complementary. Works with tactical or navigation-grade inertial system haven proven the interests

[21]. During the last decade, the advances in low-cost MEMS have made the MEMS sensors more and more attractive for various applications such as pedestrian or vehicle navigation [1,3,13].

The general objective of this contribution is thus to investigate the navigation performance one can expect from a low-cost architecture (single-frequency receiver with low cost IMU) using carrier phase measurements in an urban canyon, where the frequency of occurrence of strong multipath environment, masking, NLOS signal tracking, interference, etc.... is adequately higher but not well known.

This paper follows up on previous work performed in [6] which assessed the possibility of achieving accurate positioning based on RTK with a low-cost single-frequency multi-constellation receiver in urban and semi-urban areas. Two main ideas were used:

- The use of multi-constellation to allow for a very tight measurement selection methodology in order to limit to the maximum extent possible the number of erroneous measurements in the PVT computation process without compromising too much the geometry. To do so, GPS and GLONASS measurements were used and rejection of outliers and re-weighting mechanisms (Danish method) of GNSS measurements were proposed.
- A PVT computation based on a KF taking inputs from code, phase, and Doppler observables, as well as from a carrier phase measurement CS monitor in order to better use the knowledge of measurements without CS in the estimation process. This monitor proved to be critical in the navigation performance. An *Integer Ambiguity Resolution* (IAR) method, consisting of the integer estimation part based on the *Least-squares AMBiguity Decorrelation Adjustment* (LAMBDA) method and the integer validation part based on Fix-Threshold Ratio Test (FT-RT), was applied.

The conclusion of [6] was that reliable low-cost precise positioning (sub-meter) was possible with very decent performance in semi-urban area, for example a beltway. However, more work was needed for deep urban conditions. Besides, the ability of having a reliable ambiguity resolution process was also questioned since it was one of the main drawback for appropriately quantifying the quality of the resulting position.

The present article provides a series of modifications to [6]:

- The use of a low-cost IMU hybridized with GNSS, to strengthen the positioning performance in favorable GNSS environment, restrict the degradation during partial or full GNSS outages;
- A new *Cycle Slip Detection and Repair* (CS-DR) mechanism is proposed to provide better and more

reliable information to the PVT Kalman Filter. For a kinematic mode in urban areas, the involvement of Doppler measurements which are vulnerable to several error sources and strongly affected by the rover dynamics will weaken the CS-DR process. Besides, it is likely that some extra knowledge of the system can be relied upon. The idea is thus to

- Benefit from the accurate system updates provided by INS navigation to detect and correct CSs;
- Separate null-CS satellites from others, and make advantage of the whole geometry to repair CSs.
- Measurement selection based on the GNSS/INS KF innovations is performed. Of particular interest is the case of NLOS signals that can contaminate the PVT without necessarily been affected by a low C/N0 or high multipath. It is also critical to evaluate if the use of the INS for CS and position computation does not provide a useless redundancy.

2 GNSS-ONLY SYSTEM

2.1 PVT-Estimation with KF

The realization of GNSS-PVT navigation is mainly based on a KF which is the most popular choice for its optimality and simplicity to implement. Compared to the Least-squares method which only relies on the measurement model, the KF also combines the information about the system dynamics.

To have an estimation of a set of parameters of interests (herein, rover position, velocity, clock delays, etc.), a functional relationship between the state parameters and the measurements must be established. The functional model is typically given in form Eq.(1):

$$y(t) = H(t) \cdot x(t) + e(t) \quad (1)$$

where:

- $y(t)$ is the measurement vector at time t ;
- $H(t)$ is the system geometry matrix at time t ;
- $x(t)$ is the system state vector at time t ;
- $e(t)$ is the measurement noise vector at time t , a zero-mean Gaussian noise with spectral density $R(t)$.

Typical system dynamics can be represented in following Eq. (2):

$$\dot{x}(t) = F(t) \cdot x(t) + G(t) \cdot w(t) \quad (2)$$

where:

- $\dot{x}(t)$ the 'dot' represents time derivative;
- $F(t)$ is the dynamic matrix at time t ;
- $G(t)$ is the process noise shaping matrix at time t ;
- $w(t)$ is the process driving noise at time t , a zero-mean Gaussian noise with spectral density matrix $Q(t)$, assumed to be un-correlated with measurement noise $e(t)$.

In GNSS PVT case, the estimation process is usually implemented in discrete time and the Extended-KF in its linearized form is here applied. Assuming the sampling time as $t_s = \frac{1}{f_s}$, the discrete linear system is given as:

$$Y_k = H_k X_k + e_k \quad (3)$$

$$X_k = \Phi_k X_{k-1} + w_k \quad (4)$$

where

- Y_k, X_k are respectively the measurement vector and the state vector at epoch k with corresponding time $t_k = t_{k-1} + t_s$;
- Φ_k is the state transition matrix from epoch $(k-1)$ to epoch k ;
- w_k is the process noise at epoch k , with covariance matrix Q_k .

The detailed expressions of Φ_k and Q_k can be obtained from following relations:

$$\Phi_k = e^{F(t_k)t_s} \approx I + F_k t_s + \frac{(F_k t_s)^2}{2} \quad (5)$$

$$Q_k \approx [\Phi_k G(t_{k-1}) Q(t_{k-1}) G^T(t_{k-1}) \Phi_k^T + G(t_{k-1}) Q(t_{k-1}) G^T(t_{k-1})] t_s / 2 \quad (6)$$

For more information about the derivation process, refer to [5,13,21,23]. Approximations made during the propagation interval t_s may not be rigorously correct, but reasonably acceptable when t_s is considerably enough small.

2.2 RTK Measurements Model

Taking advantage of the temporal and spatial correlation characteristics of most measurements errors (atmosphere delay, ephemeris errors, etc.), differential measurements w.r.t a referential IGN station are formed in order to eliminate the measurement errors. This generally gives RTK method a better performance than stand-alone GNSS [14].

Regarding differential measurements, two basic forms should be stated:

- SD: Single-differencing between receivers is referred to the difference of measurements between a pair of receivers, i.e. the rover's receiver and the reference station's receiver, sharing a common satellite.
- DD: Double-differencing is the difference between two SD measurements collected from two different satellites, but with the same pair of receivers.

Various combinations of differential measurements as KF inputs can be used with original GNSS code and carrier phase measurements. Herein, to conserve the integer nature of ambiguities and control the measurement noise level at the input, following combinations are implemented:

- GPS code measurements are single-differenced;
- GPS carrier phase measurements are double-differenced;

- GLONASS code and carrier phase measurements are single-differenced;
- Original GPS and GLONASS Doppler measurements are collected by the rover receiver.

For the reason that not all reference stations distribute raw Doppler measurements, only Doppler measurements collected by the rover is put into use.

Finally the measurement vector Y is:

$$Y = \begin{bmatrix} \Delta P^{GPS/GAL} \\ \Delta P_i^{GLO} \\ \nabla \Delta \Phi^{GPS/GAL} \\ \Delta \Phi_i^{GLO} \\ D^{GPS/GAL} \\ D_i^{GLO} \end{bmatrix} = \begin{bmatrix} \Delta \rho + c \Delta dt + \varepsilon_{\Delta P} \\ \Delta \rho + c \Delta dt + b_r + k_i b_{ICB,code} + \varepsilon_{\Delta P_i} \\ \nabla \Delta \rho + \lambda \nabla \Delta N + \varepsilon_{\nabla \Delta \Phi} \\ \Delta \rho + c \Delta dt + \lambda_i \Delta N_{i,eq} + \varepsilon_{\Delta \Phi_i} \\ \dot{\rho} + c \dot{d}_D + \varepsilon_D \\ \dot{\rho} + c \dot{d}_D + \varepsilon_{D_i} \end{bmatrix} \quad (7)$$

where

- $\Delta \rho$ is the true range difference to a common satellite between the rover and the reference;
- Δdt is the difference of clock delays between the rover and the reference, while \dot{d}_D is the clock drift of the rover side;
- b_r is the GLONASS inter-receivers hardware code bias (see following section for details);
- $b_{ICB,code}$ is the GLONASS code inter-channel bias slope (see following section for details);
- $k_i \in [-7, 6]$ is the GLONASS frequency number,
- $\lambda_i \Delta N_{i,eq} = \lambda_i \Delta N_i + k_i b_{ICB,phase}$ is the equivalent ambiguity term consisting of the true integer GLONASS SD ambiguity ΔN_i and phase ICB slope $b_{ICB,phase}$.

To reflect and benefit from the accuracy differences among code measurements, carrier phase measurements and Doppler measurements, different C/N0 related weighting algorithms based on practical data have been proposed in [6]. An illustration of the relation between SD code residual level and signal strength in a static mode is provided in Figure 1. However, tests on our data have indicated the weighting scheme being too conservative on weighting high-elevation pseudo-ranges and Doppler measurements and the reliance on high-elevation satellites over low-elevation ones is not adequate. Therefore in this paper an elevation-dependent factor $\left(\frac{\sin(T_{elev})}{\sin(elev)}\right)^2$ is applied, where T_{elev} is a constant

elevation value and $elev$ is the current elevation of the satellite in view of the rover.

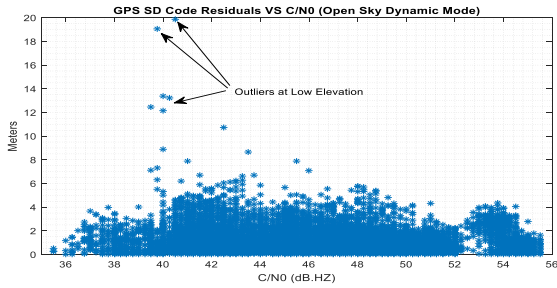


Figure 1. The Relation between GPS SD Code Residuals Level and C/N0 in a Static Environment

2.3 System States

1) Dynamic Model

Basic states are the rover position, the velocity and the acceleration. The Constant-Acceleration Model [5] is applied in this study to describe the relations among their process noises. For the acceleration process, a noise level of variance, e.g. [0.7, 0.7, 0.2] ((m/s²)²) along ENU-directions is assumed [6].

When considering a multi-GNSS system and carrier phase measurement processing, in addition to typical PVT states, the GLONASS Inter-Channel Biases (ICBs)-related parameters and carrier-phase ambiguities need to be considered in the state vector.

2) Ambiguities

Even though the integer nature of ambiguities should be benefited to shrink the navigation accuracy to cm level, the mentioned IAR method (LAMBDA+FT-RT) may provide wrong-fixings without alerts when the information provided by the KF on ambiguity estimates are not perfectly corresponding to the reality. Besides, tests in an open environment have even shown the occurrences of solution deteriorations due to wrong carrier-phase ambiguity fixing.

As the IAR is a very complex process already and that it can be the source of very compromising wrong fixing, it has been decided in a first step to only deal with float ambiguities in the PVT process. A new fixing process will be investigated and tested in later publications.

3) GLONASS ICBs

Literatures on GLONASS have shown that due to its use of *Frequency Division Multiple Access*, ICBs need to be taken into account on both pseudo-range and carrier phase observables [12,17]. Practical studies have shown that:

1. no obvious pattern of pseudo-range ICBs magnitude as a function of the frequency number is observed, however there is one on carrier phase ICBs;

2. the biases are quite independent from receivers pair to pair;
3. the pseudo-range and phase ICBs are all quite stable in time (at least on a monthly scale), which leaves a possibility of pre-calibration.

However, all previous studies are using high-quality receivers [15,26]. Among them, some are directly based on IGN stations [2,7,8,25].

Code measurements ICBs

Two static data of 3-days duration have been collected using a low-cost Ublox M8T receiver for the calibration of $b_{r,i}$, using the following GLONASS measurement model

$$\Delta P_i = \Delta \rho + c\Delta t + b_{r,i} + \varepsilon_{\Delta P_i} \quad (8)$$

Stability over days is observed. The calibration result of code ICBs is presented in Figure 2. As expected, there is no clear relation between frequency numbers and bias magnitudes. The peak-to-peak bias can reach up to 9 meters. Based on the current literature, even though the proposed algorithm uses pre-calibration, a two-state model (modeling the residual ICBs as a linear function of the GLONASS frequency index) has been implemented, as already presented in Eq. (7).

Carrier phase measurements ICBs

With the phase ICBs $b_{ICB,phase}$ in presence, the pre-calibration of carrier phase biases is necessary to benefit from the integer nature of SD ambiguities. Nevertheless, this bias will be absorbed when GLONASS ambiguities are kept float and thus no need to be pre-calibrated.

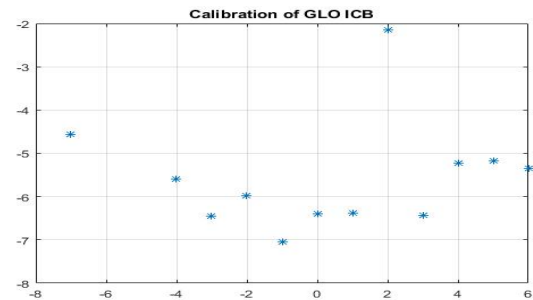


Figure 2. Estimated GLONASS Pseudo-range ICBs Depending on Frequency Numbers for a Baseline between TLSE Reference Station (Trimble Receiver) and the Ublox M8T Receiver

3 INS-ONLY SYSTEM

As mentioned earlier, the proposed architecture includes the use of a low-cost IMU. This section introduces the background on the sensor used.

In this article, all navigational parameters are resolved with respect to the local East-North-Up local frame (n-frame).

3.1 Modeling of IMU Observables

The IMU observables are typically corrupted by errors like biases, scale factor and misalignment errors. At the outputs of IMU sensors, collected raw measurements can thus be modelled as follows:

$$\begin{aligned}\tilde{f}_{ib}^b &= \mathbf{b}_a + (\mathbf{I}_3 + \mathbf{S}_a)\mathbf{f}_{ib}^b + \mathbf{w}_a \\ \tilde{\omega}_{ib}^b &= \mathbf{b}_g + (\mathbf{I}_3 + \mathbf{S}_g)\omega_{ib}^b + \mathbf{w}_g\end{aligned}\quad (9)$$

where

- \tilde{f}_{ib}^b and $\tilde{\omega}_{ib}^b$ are respectively the raw measured specific force and angular velocity expressed in body frame (b -frame);
- \mathbf{S}_a and \mathbf{S}_g are respectively the accelerometer and the gyroscope scale factors;
- \mathbf{b}_a and \mathbf{b}_g are respectively the accelerometer and the gyroscope biases;
- \mathbf{w}_a and \mathbf{w}_g are the zero-mean white Gaussian the accelerometer and the gyroscope sensor noises;
- \mathbf{I}_3 is the 3×3 identity matrix.

Biases in gyroscope and accelerometer are typically composed of two parts: **static** (known as turn-on bias, constant throughout an IMU operating period, but varying from run to run) and **dynamic** (in run bias/bias instability, varying over periods of order one minute) [14]:

$$\begin{aligned}\mathbf{b}_a &= \mathbf{b}_{as} + \mathbf{b}_{ad} \\ \mathbf{b}_g &= \mathbf{b}_{gs} + \mathbf{b}_{gd}\end{aligned}\quad (10)$$

Generally, the static parts are modelled as random constant processes (or calibrated) and the dynamic parts are represented with a first-order *Gauss-Markov* (GM) process:

$$\begin{aligned}\dot{\mathbf{b}}_a &= -1/\tau_{b_a} \cdot \mathbf{b}_a + \boldsymbol{\eta}_{b_a} \\ \dot{\mathbf{b}}_g &= -1/\tau_{b_g} \cdot \mathbf{b}_g + \boldsymbol{\eta}_{b_g}\end{aligned}\quad (11)$$

with

- τ_{b_a}, τ_{b_g} are the correlation times,
- $\boldsymbol{\eta}_{b_a}, \boldsymbol{\eta}_{b_g}$ are the GM process driving noise.

To get those key parameters of the processes, IMU data need be exploited. Different methods have been proposed, PSD method, Wavelet de-noising [10,22], autoregressive model [18], Allan Variance (AV) method, etc. The AV method is the most popular for its practical simplicity and strict systematic theories [9,10,27].

Hours of static IMU measurements have been collected with the XSENS MTi, the IMU equipment used in this study. The AV plots of the XSENS MTi gyroscope noises and accelerometer noises are given respectively in Figure 3 and Figure 4.

Two typical noises have appeared on the plots:

1. Random walk driving noise-white noise, appears on the Allan Deviation log-log plot, associated to the section with a slope of -0.5. By fitting a straight line through the slope, the corresponding value at the

cluster time $t=1s$ is denoted as N (sometimes represented by VRW ($m/s/\sqrt{Hz}$) for the accelerometer or ARW ($rad/s/\sqrt{Hz}$) for the gyroscope);

2. Bias instability (denoted as B) appears on the plot as a flat region around the minimum. The numerical minimum value is 0.664B on the curve. The correlation times is the cluster time corresponding to the minimum of plots. See Table 1 for detailed parameter readings.

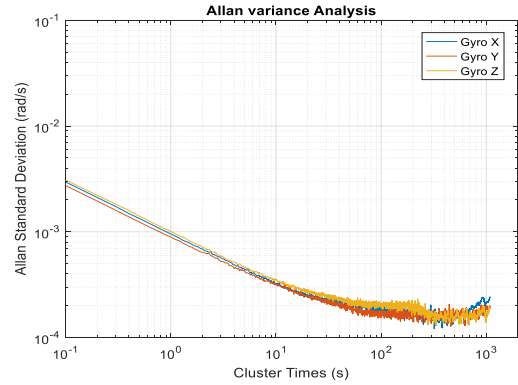


Figure 3. Allan Variance of Gyroscope Noise

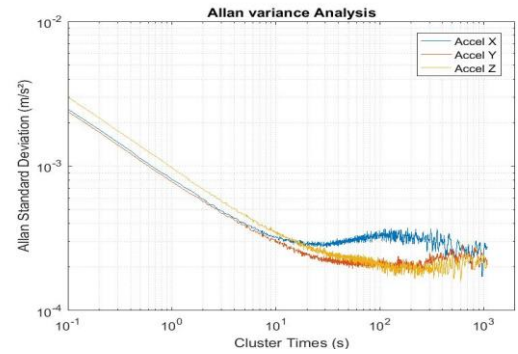


Figure 4. Allan Variance of Accelerometer Noise

Table 1. Process Noises Analysis with Allan Variance Method

MTi	Accelerometer			Gyroscope		
	x	y	z	x	Y	Z
Tc (s)	300	300	300	300	300	300
0.664	3e-4	2e-4	2e-4	1.5e-4	1.5e-4	2e-4
B	4.5181	3.012	3.012	2.259	2.259	3.012
	e-4	e-4	e-4	e-4	e-4	e-4
N	8e-4	7.8e-4	1e-3	9.5e-4	9e-4	1e-3

3.2 Equations of Motions and INS Mechanization

By having the position, the velocity and the direction cosine matrix of vehicle attitudes to describe the motion, the equations of motions under n -frame are:

$$\begin{bmatrix} \dot{\mathbf{r}}_{nb}^n \\ \dot{\mathbf{v}}_{nb}^n \\ \dot{\mathbf{C}}_b^n \end{bmatrix} = \begin{bmatrix} \mathbf{F}_{rv} \cdot \mathbf{v}_{nb}^n \\ \mathbf{C}_b^n \mathbf{f}_{ib}^b - (2\boldsymbol{\Omega}_{ie}^n + \boldsymbol{\Omega}_{en}^n) \mathbf{v}_{nb}^n + \mathbf{g}^n \\ \mathbf{C}_b^n (\boldsymbol{\Omega}_{ib}^b - \boldsymbol{\Omega}_{in}^b) \end{bmatrix}\quad (12)$$

Please refer to Annex for detailed terms expressions.

The INS mechanization equations are a set of equations used to obtain useful navigation solution from IMU measurements. Basic steps are in order: 1. Correction of raw IMU measurements with information on previous biases and scale factors estimates; 2. Attitudes computation from quaternion update for its simplicity and clarity in computational manipulation; 3. Update of velocity by adding the velocity increment $\Delta \mathbf{v}_{nb}^n = \dot{\mathbf{v}}_{nb}^n \Delta t$; 4. Update of position. Δt is used to show the INS update temporal interval, i.e. 0.01s. Detailed descriptions of this typical process are referred to [19]. No more descriptions are dressed here.

3.3 INS Error States Model

1) Notations of error states

Error states are defined as differences between states estimates (terms with ‘hat’) and their true values with following notations:

$$\left\{ \begin{array}{l} \delta \mathbf{r}_{nb}^n = \hat{\mathbf{r}}_{nb}^n - \mathbf{r}_{nb}^n \\ \delta \mathbf{v}_{nb}^n = \hat{\mathbf{v}}_{nb}^n - \mathbf{v}_{nb}^n \\ \mathbf{C}_b^n = \hat{\mathbf{C}}_b^n - \delta \mathbf{C}_b^n = (\mathbf{1} + \mathbf{E}) \hat{\mathbf{C}}_b^n \\ \delta \mathbf{b}_a = \mathbf{b}_a - \hat{\mathbf{b}}_a \\ \delta \mathbf{S}_a = \mathbf{S}_a - \hat{\mathbf{S}}_a \\ \delta \mathbf{b}_g = \mathbf{b}_g - \hat{\mathbf{b}}_g \\ \delta \mathbf{S}_g = \mathbf{S}_g - \hat{\mathbf{S}}_g \end{array} \right. \quad (13)$$

with $\mathbf{E} = [\delta \boldsymbol{\psi} \wedge] = \begin{bmatrix} 0 & \delta \varphi_{nb} & \delta \phi_{nb} \\ -\delta \varphi_{nb} & 0 & -\delta \theta_{nb} \\ -\delta \phi_{nb} & \delta \theta_{nb} & 0 \end{bmatrix}$, the skew-symmetric matrix of attitudes errors in order $\delta \boldsymbol{\psi} = [\delta \theta_{nb}, \delta \phi_{nb}, -\delta \varphi_{nb}]^T$.

2) Error States Dynamics

The compact representation of INS error states dynamics is obtained by doing the perturbation analysis of Eq.(12):

$$\begin{aligned} & \begin{bmatrix} \delta \dot{\mathbf{r}}_{nb}^n \\ \delta \dot{\mathbf{v}}_{nb}^n \\ \delta \dot{\boldsymbol{\psi}} \end{bmatrix} \\ &= \begin{bmatrix} \mathbf{F}_{rr} & \mathbf{F}_{rv} & \mathbf{0}_3 \\ \mathbf{F}_{vr} & \mathbf{F}_{vv} & \mathbf{F}_{ve} \\ \mathbf{F}_{er} & \mathbf{F}_{ev} & \mathbf{F}_{ee} \end{bmatrix} \begin{bmatrix} \delta \mathbf{r}_{nb}^n \\ \delta \mathbf{v}_{nb}^n \\ \delta \boldsymbol{\psi} \end{bmatrix} \\ &+ \begin{bmatrix} \mathbf{0}_3 & \mathbf{0}_3 & \mathbf{0}_3 & \mathbf{0}_3 \\ \mathbf{C}_b^n & \mathbf{0}_3 & \mathbf{C}_b^n \mathbf{F}_b & \mathbf{0}_3 \\ \mathbf{0}_3 & -\mathbf{C}_b^n & \mathbf{0}_3 & -\mathbf{C}_b^n \mathbf{W}_b \end{bmatrix} \begin{bmatrix} \delta \mathbf{b}_a \\ \delta \mathbf{b}_g \\ \delta \mathbf{S}_a \\ \delta \mathbf{S}_g \end{bmatrix} \\ &+ \begin{bmatrix} \mathbf{0}_3 \\ \mathbf{C}_b^n \boldsymbol{\eta}_a \\ -\mathbf{C}_b^n \boldsymbol{\eta}_g \end{bmatrix} \end{aligned} \quad (14)$$

$$\left\{ \begin{array}{l} \delta \dot{\mathbf{b}}_a = \frac{-1}{\tau_{ba}} \delta \mathbf{b}_a + \boldsymbol{\eta}_{ba} \\ \delta \dot{\mathbf{b}}_g = \frac{-1}{\tau_{bg}} \delta \mathbf{b}_g + \boldsymbol{\eta}_{bg} \\ \delta \dot{\mathbf{S}}_a = \frac{-1}{\tau_{sa}} \delta \mathbf{S}_a + \boldsymbol{\eta}_{sa} \\ \delta \dot{\mathbf{S}}_g = \frac{-1}{\tau_{sg}} \delta \mathbf{S}_g + \boldsymbol{\eta}_{sg} \end{array} \right. \quad (15)$$

Please refer to Annex for detailed terms expressions.

3) Process noise of GM

As mentioned earlier, biases of gyroscope and accelerometer are modeled as GM processes. The PSDs corresponding to the process-driving noise $\boldsymbol{\eta}_{ba}$, $\boldsymbol{\eta}_{bg}$ are already gathered in Table 1, denoted by term B.

The covariance value in discrete time of a GM process-driving noise is then

$$\mathbf{Q}_{GM} = \left(2 \frac{B^2}{\tau_c} \right) * \Delta t \quad (16)$$

The scale factors are also normally modeled as GM processes with intuitively a much lower process-driving noise level, i.e. 1e-14 and a longer correlation times, i.e. 3hrs. Static data over a duration of several days would be needed to study scale factors through the AV method.

4) Process noise of position, velocity and attitudes

$\boldsymbol{\eta}_g$, $\boldsymbol{\eta}_a$ are white noises related to IMU measurements. The covariance value in discrete time is thus, with N obtained from AV study

$$\mathbf{Q}_{WN} = \frac{N^2}{\Delta t} = \left(\frac{N}{\Delta t} \right)^2 * \Delta t \quad (17)$$

According to Eq.(14), the process noises related to the velocity errors and attitudes errors are holding discrete-time covariance values in formula:

$$\mathbf{Q}_{\delta v_{nb}^n} = \mathbf{C}_b^n \left(2B_a^2 \frac{\Delta t}{\tau_c} + N_a^2 / \Delta t \right) (\mathbf{C}_b^n)^T \quad (18)$$

$$\mathbf{Q}_{\delta \boldsymbol{\psi}} = \mathbf{C}_b^n \left(2B_g^2 \frac{\Delta t}{\tau_c} + N_g^2 / \Delta t \right) (\mathbf{C}_b^n)^T \quad (19)$$

The discrete-time covariance of position process noises is derived from the position-velocity process relation, taking 1-D for instance [5]:

$$\mathbf{Q}_{\delta p_v} = \begin{bmatrix} \frac{1}{3} \mathbf{Q}_{\delta v_{nb}^n} \Delta t^2 & \frac{1}{2} \mathbf{Q}_{\delta v_{nb}^n} \Delta t \\ \frac{1}{2} \mathbf{Q}_{\delta v_{nb}^n} \Delta t & \mathbf{Q}_{\delta v_{nb}^n} \end{bmatrix} \quad (20)$$

4 GNSS/INS TIGHT INTEGRATION

In this scheme, the closed-loop tightly coupling (TC) is chosen over the loose coupling for two main reasons:

- to bound the degradation of the low-quality MEMS;
- to maintain the performance during partial or full GNSS outages which can be quite often in urban canyons.

4.1 State Dynamics

Compared to the GNSS-only navigation, the IMU sensor error states need also be considered. The full error state vector is denoted as

$$X^n = (\delta r_{nb}^n; \delta v_{nb}^n; \delta \psi; \delta b_a; \delta b_g; \delta S_a; \delta S_g; \delta clk; \delta Amb; \delta ICB)^T$$

1) Process noise of clock-related states

The receiver clock model applied here is referred to [11], a two-parameter model of clock delay and clock drift. The covariance matrix of process noise is

$$Q_{clk(s)} = \begin{bmatrix} \frac{h_0}{2}t_s + 2h_{-1}t_s^2 + \frac{2}{3}\pi^2 h_{-2}t_s^3 & h_{-1}t_s + \pi^2 h_{-2}t_s^2 \\ h_{-1}t_s + \pi^2 h_{-2}t_s^2 & \frac{h_0}{2t_s} + 4h_{-1} + \frac{8}{3}\pi^2 h_{-2}t_s \end{bmatrix}$$

with h_0, h_{-1}, h_{-2} parameters related to the receiver clock quality performance.

In the following table are the typical values for various types of receiver clock [5]. A TCXO-type oscillator is incorporated in the Ublox receiver, while a more stable OCXO-type oscillator is used by the TLSE Trimble NetR9 receiver.

Table 2. Parameters for Clock Modeling

Types	TCXO*	OCXO*
Parameters		
h_0	2e-19	2e-25
h_{-1}	7e-21	7e-25
h_{-2}	2e-20	6e-25

*TCXO: temperature compensated crystal oscillator

*OCXO: ovenized crystal oscillator, temperature controlled

4.2 Lever-arm Effect on Error States Dynamics

While considering the integration between INS and GNSS, the lever-arm effect between the 2 systems should always be taken into account.

Assuming l^b the lever-arm vector resolved in b-frame, representing the vector from the INS center O_b to the GNSS antenna phase center O_B , the position and velocity relations between those two origins are:

$$\begin{aligned} r_{O_B}^n &= r_{O_b}^n + C_b^n l^b \\ v_{O_B}^n &= v_{O_b}^n + C_b^n [w_{nb}^b \times] l^b \end{aligned} \quad (21)$$

where $\Omega_{nb}^b = [w_{nb}^b \times]$, for detailed formula see Annex.

With perturbation analysis, we have

$$\delta r_{O_B}^n = \delta r_{O_b}^n + [C_b^n l^b \times] \delta \psi \quad (22)$$

$$\begin{aligned} \delta v_{O_B}^n &= \delta v_{O_b}^n + \{ [C_b^n \Omega_{ib}^b l^b \times] \\ &\quad - (\Omega_{en}^n + \Omega_{ie}^n) [C_b^n l^b \times] \} \delta \psi \\ &\quad - C_b^n [l^b \times] (\delta b_g \\ &\quad + \text{diag}(w_{ib}^b) \delta S_g) \end{aligned}$$

4.3 GNSS Measurement Selection

Different from loosely coupling, where differences between INS-derived states and GNSS-derived states are used as input, TC is using measurements differences between INS and GNSS as input for TC KF. Thus, it is essential to ensure the GNSS measurements quality. To remove measurements that are most likely severely degraded by multipath or NLOS effects, an a-priori elevation mask and C/N0 mask are applied for all measurements. The choice of the masks values is a compromise between a strong geometry and high quality measurements. Different values have been tested and an interesting compromise seems to be an elevation mask set to be 10° and a C/N0 mask is set to be 35dB.Hz.

Besides this a priori GNSS measurement selection, another measurement selection scheme is applied based on the KF innovations. In constrained environment, GNSS measurements are more vulnerable to non-Gaussian error sources (e.g., NLOS, multipath) [16]. The detection of blunders is necessary to ensure a reliable PVT solution [21]. Compared to the GNSS-only system, the state propagation noise is smaller in the GNSS/INS integration case, thus providing a more efficient detection and identification of outliers. The proposed Innovation-Test is detailed in following three steps: detection, identification and adaptation.

1) Detection

With state estimates from the previous epoch, the measurement innovations provides an indication of whether the current epoch measurements and state estimates are consistent via a global test [14]. The null hypothesis is that no measurement blunder exists. The global test will check the overall validity of the null hypothesis.

For current epoch $k + 1$, the KF innovation vector $\tilde{Y}_{k+1} \in \mathbb{R}^p$ is defined as

$$\tilde{Y}_{k+1} = Y_{k+1} - \hat{Y}_{k+1} = Y_{k+1} - H_{k+1} \hat{X}_{k+1|k}$$

and its vc-matrix is

$$C_{k+1} = H_{k+1} P_{k+1|k} H_{k+1}^T + R_{k+1}.$$

$\hat{X}_{k+1|k}$ is the state propagation results after going through the INS mechanization equations.

Under the null hypothesis, these innovation components should follow zero-mean Gaussian distributions and the test statistic Summation of the Squared Errors (SSE) is following a chi-square distribution with p degrees of freedom,

$$SSE = \tilde{Y}_{k+1}^T * (C_{k+1})^{-1} * \tilde{Y}_{k+1}$$

The comparison of the test statistic SSE with a critical threshold T will tell whether the null hypothesis is confirmed. The threshold value depends on a pre-defined significance level (i.e., the probability of false alarm) α_1 .

2) Identification

When the null hypothesis is rejected in the global test, local tests are performed to identify the outliers. The local test is performed on each innovation $i \in [1, 2, \dots, p]$, with the test statistic defined as

$$|\mathbf{t}_{k+1,i}| = \left| \frac{\tilde{Y}_{k+1,i}}{(C_{k+1})_{ii}} \right| \geq N_{1-\frac{\alpha_2}{2}}$$

with $N_{1-\frac{\alpha_2}{2}}$ is the decision threshold, α_2 (e.g., 0.03) the probability of false alarm. This local test can be regarded as the testing of the single-blunder hypothesis [21].

3) Adaptation

Each time the global test fails, the local test is performed on each innovation component:

- When multiple outliers are identified by the local tests, only the one with the maximum $|\mathbf{t}_{k+1,i}|$ is rejected to avoid the case where a blunder is large enough to cause multiple local failures.
- When there is no outlier identified, still the innovation with the maximum $|\mathbf{t}_{k+1,i}|$ is rejected.

The global test is always re-run until it succeeds to ensure the integrity among innovations.

Beside the pseudo-range and Doppler observables, carrier-phases are taken into account in the measurement selection to detect big CS on the reference-side.

4.4 CS Detection and Repair

The proposed KF scheme assumes that the carrier phase measurements have a constant carrier phase ambiguity. However, it is well known that this does not necessarily hold for very long especially in an urban environment where frequent CSs occur. However, assuming that a CS occurs at each epoch is detrimental to the PVT algorithm accuracy performance since it implies a constant re-estimation of the float ambiguity states without benefiting from their potential continuity. It is however the least risky.

As a consequence, it might be important to closely monitor the occurrence of data outage or CS continuously to follow the continuous-phase ambiguity model with confidence. The aim of a CS-DR scheme is thus to detect the occurrence of CS and to enable the continuous use of constant carrier phase ambiguity when no CS is detected (either to be able to fix it, or to be able to use its accurately-estimated fixed value). Beside the proposed CS-DR scheme, loss of lock indicators (LLI) provided by receivers are also taken into account.

Since it can be anticipated that CS do not generally occur on all satellites at a given epoch, it is important to be able to separate the phase measurements with CS from the phase measurements without CS. To do so, a separation based on a phase prediction test and Chi-square test (referred later to Step 1 and Step 2) between highly potentially and hardly CS-contaminated satellites will strengthen the system [24].

The proposed CS-DR scheme is based on the following system:

$$\begin{cases} \delta P_{cs}^i = \frac{D^i(k) + D^i(k-1)}{2} \cdot t_s = \delta\rho + \delta dt + \varepsilon_{\delta P_{cs}^i} \\ \delta\Phi_{cs}^i = \Phi^i(k) - \Phi^i(k-1) = \delta\rho + \delta dt + CS_i \cdot \lambda_i + \varepsilon_{\delta\Phi_{cs}^i} \end{cases}$$

where

- $\delta P_{CS}^i [m]$ is the pseudo-range variation between two consecutive epochs k and $(k-1)$, determined by the product of the average Doppler observable and the time interval t_s ;
- $\delta\Phi_{cs}^i [m]$ is the difference between two consecutive carrier-phase observables;
- δdt is the difference between rover clock delays of two successive epochs, the unit is in meter;
- $CS_i [cycle]$ is the integer CS.

Considering a high rate system (t_s is less than 1s), the difference between measurements δP_{CS}^i and $\delta\Phi_{cs}^i$ will be the CS if it occurs.

The geometry matrix comes from the linearization of measurements system, with $POS_{sat}^i(\blacksquare)$ the position of satellite i at epoch \blacksquare , $POS(\blacksquare)$ the rover's position at epoch \blacksquare , $\delta X(\blacksquare)$ the between-epochs variation of the rover's position and $e^i(\blacksquare)$ the unit vector directing from the rover to the satellite at epoch \blacksquare :

$$\begin{aligned} \delta\rho &= \rho^i(k) - \rho^i(k-1) = e^i(k)[POS_{sat}^i(k) - POS(k)] \\ &\quad - e^i(k-1)[POS_{sat}^i(k-1) - POS(k-1)] \\ \delta\rho + e^i(k-1)[POS_{sat}^i(k-1) - POS(k-1)] \\ &= e^i(k)[POS_{sat}^i(k) - POS(k-1)] - e^i(k)\delta X(k) \end{aligned}$$

Therefore, with measurements corrected by $\delta\rho_{corr} = e^i(k)[POS_{sat}^i(k) - POS(k-1)] - e^i(k-1)[POS_{sat}^i(k-1) - POS(k-1)]$, the matrix representation becomes:

$$Y(k) = \begin{bmatrix} \delta P_{cs,corr}^i \\ \delta\Phi_{cs,corr}^i \end{bmatrix} = H \cdot \begin{bmatrix} \delta X(k) \\ \delta dt \\ CS \end{bmatrix} + \varepsilon$$

$$H = \begin{bmatrix} -e^1(k) & 1 & 0 & \dots & 0 \\ \vdots & \vdots & \vdots & \ddots & \vdots \\ -e^n(k) & 1 & 0 & \dots & 0 \\ -e^1(k) & 1 & \lambda_1 & \dots & 0 \\ \vdots & \vdots & \vdots & \ddots & \vdots \\ -e^m(k) & 1 & 0 & \dots & \lambda_m \end{bmatrix}$$

To take advantage of the information on states estimates $\begin{bmatrix} \hat{X}(k) \\ \widehat{dt}_D \end{bmatrix}_{INS}$, supplementary constraints based on position and clock shift estimates are always considered:

$$Y_{supp,INS}(k) = \begin{bmatrix} \hat{X}(k) - X(k-1) \\ \widehat{dt}_{D,t_s} \end{bmatrix}.$$

The subscript ‘INS’ and the ‘hat’ mean that the terms are updated states estimates coming out of the INS navigation process, based on previous TC hybridization.

The whole CS-DR process follows 4 steps in order:

Step 1. Raw CS detection test

The δP_{CS}^i can also be considered as the prediction of $\delta\Phi_{CS}^i$ when no CS occurs. A phase prediction test as follows will detect large CS occurrences:

$$H_0: t_{CS} = |\delta\Phi_{CS}^i - \delta P_{CS}^i| \leq T * \sigma_{t_{CS}}$$

The capacity of the test depends on the measurement accuracy $\sigma_{t_{CS}}$ and the threshold T defined by a tolerable false alarm rate α .

Step 2. CS-free measurements confirmation test

Following the Step 1, a separation of satellites into two sub-groups F and S is done. The letter ‘ F ’ signifies fail-passing the test H_0 and reversely, the letter ‘ S ’ is for success.

If Group S is populated by less than 5 measurements, it is augmented by the measurements that led to the 5 smallest value of $|\delta\Phi_{CS}^i - \delta P_{CS}^i|$.

A Chi-square test is conducted on Group S to confirm that the measurements of group S are CS-free. This Chi-square test is based on the assumption that $\delta\Phi_{CS}^i$ has no CS. As a consequence, the following system using only measurements of Group S is solved based on weighted LS:

$$Y_S = [\delta\Phi_{CS}^i] = H. \begin{bmatrix} \delta X(k) \\ \delta dt \end{bmatrix} + \varepsilon, i \in S$$

The sum of the squared phase measurements residuals should follow a Chi-square distribution. Thus a comparison of the test statistics to a threshold defined by the significance level will conclude whether the null-CS is true or not.

If the test is passed, all members of Group S are assumed CS-free.

Step 3. Converging with Group F

Following the test result in step 2, two cases can occur:

a. Satellites in Group S are CS-free.

In this case, $\delta\Phi_{CS,i \in S}^i$ will serve as precise measurements to strengthen the model. Only satellites in Group F are assumed to be CS-contaminated. Thus, the measurement model is

$$Y = \begin{bmatrix} \delta\Phi_{CS,i \in S}^i \\ \delta P_{CS,i \in F}^i \\ \delta\Phi_{CS,i \in F}^i \end{bmatrix} = H. \begin{bmatrix} \delta X(k) \\ \delta dt \\ CS_F \end{bmatrix} + \varepsilon$$

b. Satellites in Group S and F are all potentially CS-contaminated.

This time, these two groups are gathered. Instead of the state vector CS_F only for group F , a state vector including all CS needs to be resolved. The new measurement model including the CS state is:

$$Y = \begin{bmatrix} \delta P_{CS}^i \\ \delta\Phi_{CS}^i \end{bmatrix} = H. \begin{bmatrix} \delta X(k) \\ \delta dt \\ CS_i \end{bmatrix} + \varepsilon, i \in F \cup S$$

In cases a and b, the estimates of the CS are calculated via a WLS filter, noted as

$$\widehat{CS} = \begin{bmatrix} \widehat{CS}_1 \\ \widehat{CS}_2 \\ \vdots \\ \widehat{CS}_n \end{bmatrix}$$

Step 4. Information passed to the TC KF

There are thus 2 possible results of CS-DR:

- No CS for Group S , and only a float estimation of the CS for Group F ;
- Only a float estimation of the CS for all satellites.

In all cases, the carrier phase measurements used in the TC KF are corrected accordingly.

For the ambiguity states of the satellites without CS or a fixed integer CS, a very small process noise (e.g. 1e-8 [cycle²]) is applied. On the other hand, the covariance of ambiguity states associated to only an estimated float CS are largely inflated to represent the uncertainty of the CS estimation (a typical value of e.g. 30² [cycle²] is used).

4.5 Constraints

Various constraints can be applied in TC KF to strengthen the performance. Among those, ZUPT, NHC and ZARU are used herein.

1) Zero Velocity Update

Zero velocity update (ZUPT or ZVU) is interesting to limit the drift of the solution when the immobility of the vehicle is detected. An immobility test thus needs to be conducted.

a) Detection of immobility

In [4], the vehicle is assumed to be stationary when the velocity is under a certain threshold. The threshold value needs to be determined with the velocity information during a calibration campaign, where the vehicle is known to be stationary. According to [1,14], when all velocities are under 0.5m/s (a threshold tested in various environments), the standard deviation of IMU accelerometer measurements can be used to confirm the motionless of the vehicle. The perturbation level of accelerometer measurements in stationary mode differs from the kinematic mode. Therefore, the performance (standard deviation) of accelerometer measurements in stationary mode $\sigma_{acc,0}$ need be analyzed in a prior phase. In this article, the immobility detection scheme with a confirmation scheme based on inertial raw measurements is applied. The immobility is assumed present during T_{imm} only in case that all velocities during the interval

T_{imm} are less than 0.5 m/s, and the StdDev of measured forces is less than $3\sigma_{acc,0}$.

b) Measurement model

When an immobility is confirmed, the ZUPT constraint is modeled as,

$$y_{ZUPT} = \begin{bmatrix} \hat{v}_x^b - 0 \\ \hat{v}_y^b - 0 \\ \hat{v}_z^b - 0 \end{bmatrix} = (\hat{C}_b^n)^T \delta v_{nb}^n - (\hat{C}_b^n)^T [\hat{v}_{nb}^n \times] \cdot \delta \psi \quad (23)$$

The corresponding design matrix is

$$H_{ZUPT} = \begin{bmatrix} 0_3, (\hat{C}_b^n)^T, -(\hat{C}_b^n)^T [\hat{v}_{nb}^n \times], 0_{3 \times (N-9)} \end{bmatrix} \quad (24)$$

The measurement uncertainty put on forward-direction speed is simply 0.5m/s.

2) Non-Holonomic Constraint

The Non-Holonomic constraint (NHC) describes the fact that generally the lateral and vertical velocities are negligible compared to the straightforward velocity. This hypothesis does not hold if the vehicle is sliding laterally or jumping.

This constraint is always active in this study.

The NHC is modeled as

$$y_{NHC} = \begin{bmatrix} \hat{v}_x^b - 0 \\ \hat{v}_z^b - 0 \end{bmatrix} \quad (25)$$

Compared to the ZUPT, the design matrix H_{NHC} omits the second line of the matrix H_{ZUPT} :

$$H_{NHC} = H_{ZUPT}([1, 3], :) \quad (26)$$

The measurement noise covariance is adjusted empirically to account for the velocity uncertainty into the vehicle motion.

The StdDev of the measurements noise is set empirically to be $[0.04, 0.08] * Speed$.

3) Zero Angular Rate Update

The Zero Angular Rate Update (ZARU) constraint assumes that the angular rate should also be null when the vehicle is confirmed in stationary mode, the same detection condition as ZUPT.

The constraint measurements are given by

$$y_{ZARU} = \begin{bmatrix} \hat{w}_{ib,x}^b - 0 \\ \hat{w}_{ib,y}^b - 0 \\ \hat{w}_{ib,z}^b - 0 \end{bmatrix} = \delta w_{ib}^b = \delta b_g \quad (27)$$

The geometry matrix is:

$$H_{ZARU} = [0_3, 0_3, 0_3, 0_3, I_3, 0_{3 \times (N-15)}] \quad (28)$$

The measurement noise covariance level depends on the sensor vibration and other disturbances. Besides, higher weight is put on the measurement around the yaw axis as the yaw axis ($\hat{w}_{ib,z}^b$) is less affected by disturbances than the other two directions [14].

5 TESTS AND RESULTS

5.1 Test Set Up

The data used for this study was collected in Toulouse semi-urban area (Data 1) and downtown (Data 2) by a Ublox M8T receiver at 1 Hz with a patch antenna and the Xsens Mti IMU [28] at 100 HZ. The reference trajectories were provided by the NovAtel SPAN equipment, which tightly integrated the L1/L2 GNSS measurements with tactical grade IMU, on multi-baseline post-processing RTK mode.

The Data 1 was collected when the vehicle was driven from ENAC to the city center along the Canal de Midi. The whole trajectory in Google Earth is represented in Figure 5. The reference trajectory was provided with cm-level accuracy as indicated in Figure 6. The maximum standard deviation values, up to 10 cm, occur around 500 epochs, which correspond also to the zone having minimum visible satellites in Figure 7. The environment is quite favorable with at least 10 satellites in view for most of time.

The Data 2 was collected around the city center. The whole trajectory in Google Earth is represented in Figure 8. A dm-level trajectory accuracy was obtained as shown in Figure 9. The number of visible satellites is indicated in Figure 10. A clear uncertainty increase on the position solution was observed during the section where the number of satellites was less than 6.

As our goal is to provide reliable solutions for ground vehicles, only the horizontal performance is exploited in following section.



Figure 5. Trajectory in Google Earth and a Typical Picture of Street View by the Google Street View (Data 1).

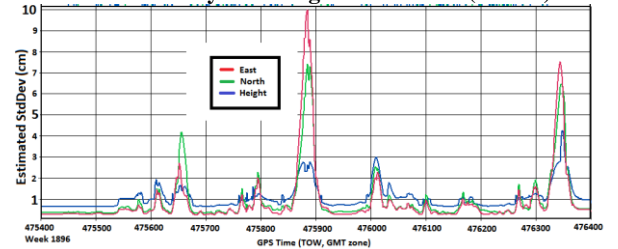


Figure 6. Position Estimated Standard Deviation in the ENU Directions of the Reference Trajectory (Data 1)

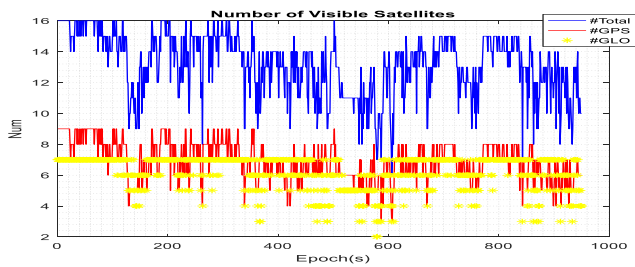


Figure 7. Number of Visible Satellites along the Trajectory (Data 1)



Figure 8. Trajectory in Google Earth and a Typical Picture of Street View by the Google Street View (Data 2).

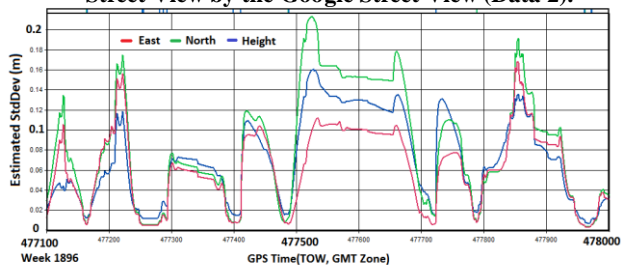


Figure 9. Position Estimated Standard Deviation in the ENU Directions of the Reference Trajectory (Data 2)

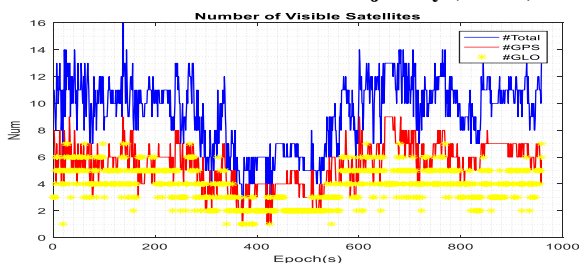


Figure 10. Number of Visible Satellites along the Trajectory (Data 2)

5.2 Test Results

Three navigation modes are presented in this section for both data campaigns. The 1st mode is denoted as ‘Float RTK’ mode, where observables of both GPS and GLONASS constellations are all employed, while in the 2nd mode ‘DGNSS+INS (Code + Doppler)’ GNSS is tightly coupled with INS, and carrier phase measurements are excluded. The word ‘float’ indicates that the ambiguities are kept float. The term T_{elev} mentioned in section 2.2 is set to be 25°. The probabilities of false alarm for outliers detection and identification are respectively 0.2 and 0.03. The 3rd mode ‘Float RTK+INS’ is taking the TC into account during CS-DR.

First of all, the performance analysis starts with Data 1. The HDOP information of Data 1 is presented in Figure 2Figure 11. A good geometry environment in general is remarked in Data 1. The mean HDOP value is around 0.8, and minimum and maximum values are separately 0.66 and 1.65. The Innovation test has detected code and Doppler outliers in 1.7% of total epochs, mostly are Doppler observables.

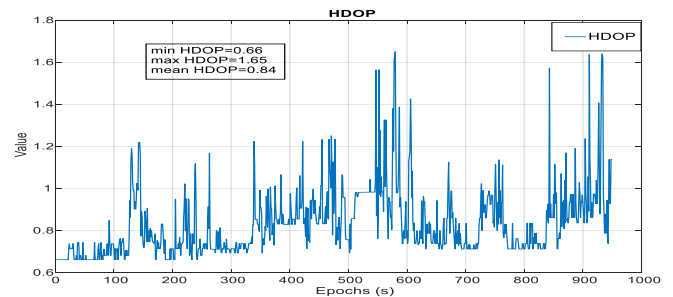


Figure 11. HDOP Values of Data 1 (with minimum, maximum, and mean HDOP values)

The key performance parameters in position domain of Data 1 and Data 2 are all listed in Table 3. To provide a complete vision in horizontal position domain, 68 percentile, 95 percentile and 99 percentile of positioning errors are provided. In Figure 13 are illustrated temporal positioning errors with Data 1. Big positioning biases, comparable to the rest epochs, are noticed from 500 to 600 epochs. This fact is consistent with the HDOP information. When the number of visible satellites decreases, the position errors in Figure 13 increase correspondingly, which indicates the capability decrease of outliers-exclusion and the influence of geometry in PVT solution.

A compromise between high CS detection rate and availability of the CS-free satellite should be made when carrier phases are considered. A false alarm rate of 0.003 is chosen for step 1 in CS-DR and a much higher one of 20% is used in step 2 of section 4.4 to give minimum margin for CSs. Besides, an absolute value of 1 cycle is added to strengthen the detection of CSs.

CSs are detected over 856 epochs, with the number of CS-contaminated satellites ranging from 1 to 16, the total number of visible satellites in related epoch. Actually, according to LLI information, the number of epochs with CS-contaminated satellites arrives already reaches up to 838. A severe CS condition is dealt with in Data 1. However, the number of epochs where there are more than 5 CS-free satellites is also high, 539 epochs. The original intention to profit from CS-free is feasible. The explicit CS-free rates associated to each satellite are listed in Table 4, in which the first line contains the mean elevation in (°) for each satellite. The term ‘Rate 1’ indicates the CS-free rate in 1st mode, and accordingly ‘Rate 3’ is for 3rd mode. Satellites with lower elevation tend to suffer more from CSs.

Table 3. Performance Summary of Different Navigation Modes

	Horizontal Position Error (m)		
	68 Percentile	95 Percentile	99 Percentile
	1st Mode: Float RTK		
Data 1	1.05	1.76	2.12
Data 2	2.14	3.82	5.6
2nd Mode: GNSS+INS (Code + Doppler)			
Data 1	0.95	1.58	2.11
Data 2	2.25	3.46	4.68
3rd Mode: Float RTK+INS			
Data 1	1.18	1.86	2.04
Data 2	2.62	3.68	4.5

Table 4. CS-free Rate of Each Satellite in Data 1

Sat	6	10	12	14	15	17
Elev(°)	11	10	79	26	22	9
Rate 1	0.03	0.07	0.57	0.31	0.3	0.18
Rate 3	0.03	0.069	0.56	0.3	0.3	0.18
Sat	19	24	25	32	33	40
Elev	30	66	45	30	29	28
Rate 1	0.32	0.55	0.39	0.43	0.42	0.3
Rate 3	0.32	0.54	0.38	0.42	0.41	0.3
Sat	41	42	43	51	52	-
Elev	34	61	24	38	40	-
Rate 1	0.43	0.57	0.29	0.4	0.54	-
Rate 3	0.42	0.56	0.29	0.39	0.53	-

The TC with low-cost MEMS in 2nd mode does not bring remarkable improvements in position solution when the GNSS measurements are in big number as in Figure 14. However, as expected, the undermining rate of position solutions has decreased around 100 epochs and 500 epochs in Figure 14, where the numbers of satellites decrease. We believe that no potential CS has been missed out during the CS detection. However, due to frequent CS detection by the proposed CS-DR, the consideration of carrier phases does not improve the positioning performance. Nevertheless, the two algorithms provide consistent bounds.

When the 3rd mode is applied with same CS-DR parameters as 1st mode, the number of epochs when CSs are detected and when CS-free exist has slightly changed to 855 and 528. Compared to 1st mode, another 11 epochs where there were in 1st mode CS-free satellites are considered CS corrupted. The change of CS-free rate compared to 1st mode is negligible. Finally, the integration with low-cost INS does not bring a significant improvement, probably due to a good GNSS-only CS detection.

The Data 2 was collected in a denser urban environment than Data 1. In Figure 10, there are in total only around 6 satellites in view from 400 to 600 epochs. The temporal HDOP values are illustrated in Figure 12 with mean HDOP up to 2.5.

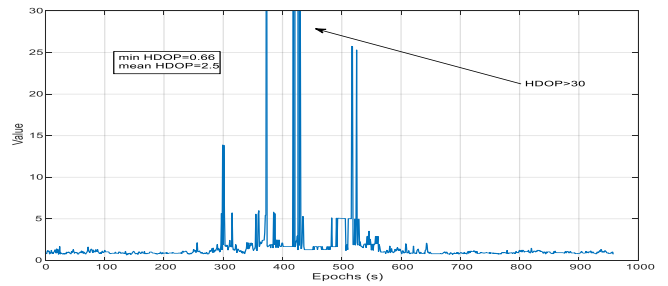


Figure 12. HDOP Values of Data 2 (with minimum and mean HDOP values)

In 1st mode with Data 2, same CS-DR related parameters are applied as with Data 1. CSs are detected over 732 epochs and more than 5 CS-free satellites are available around 373 epochs. Explicit CS-free rate for each satellite is listed in Table 5. A much higher bias level is finally observed in Figure 16. For time zones with peak HDOP values, e.g. around 400 epoch, the position bias increases correspondingly.

For Data 2, the improvement brought by the INS in Figure 17 is around the area where GNSS measurement are in small amount, e.g. between 400 and 500 epochs. And, the temporal position errors are smoother. When 3rd mode is applied, compared to 1st mode, there is rarely performance improvement of the CS-DR scheme.

In Figure 18, several biased zones are remarked, e.g. between 100 and 200 epoch, before 500 epoch. During those intervals, the stationary of the vehicle is detected, and more CS-free satellites are in presence. This fact leads to the whole system stuck with the previously estimated biased ambiguities.

Table 5. CS-free Rate of Each Satellite in Data 2

Sat	2	6	12	14	15	19
Elev(°)	16	15	74	35	9.8	21
Rate 1	0.31	0.26	0.42	0.35	0.51	0.31
Rate 3	0.31	0.26	0.42	0.35	0.51	0.32
Sat	24	25	29	32	33	34
Elev	54	56	22	38	27	11
Rate 1	0.41	0.39	0.43	0.28	0.42	0.15
Rate 3	0.42	0.39	0.43	0.28	0.41	0.15
Sat	40	41	42	43	51	52
Elev	16	24	62	34	30	53
Rate 1	0.47	0.52	0.38	0.31	0.37	0.41
Rate 3	0.47	0.52	0.38	0.31	0.37	0.41

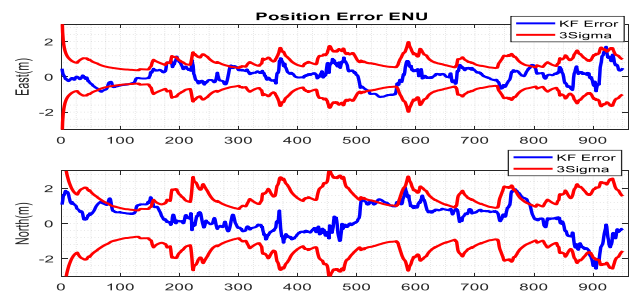


Figure 13. Estimated Horizontal Error in 1st Mode of Data 1.

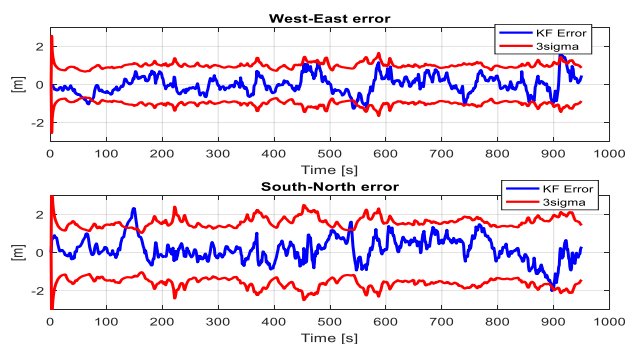


Figure 14. Estimated Horizontal Error in 2nd Mode of Data 1.

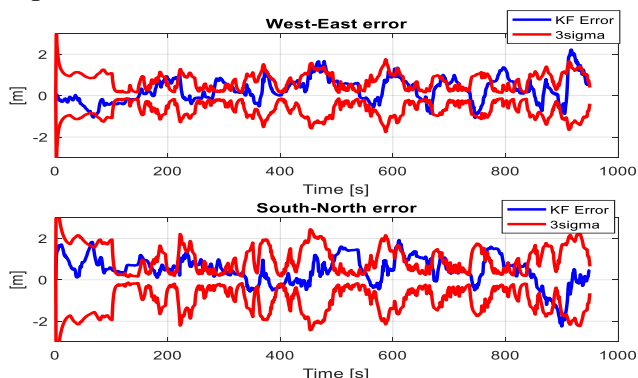


Figure 15. Estimated Horizontal Error in 3rd Mode of Data 1.

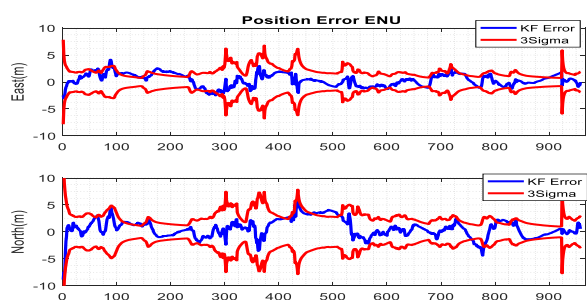


Figure 16. Estimated Horizontal Error in 1st Mode of Data 2.

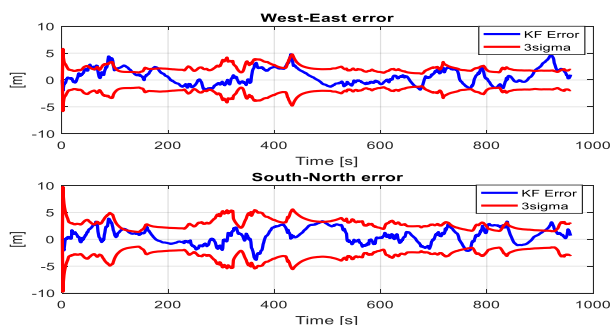


Figure 17. Estimated Horizontal Error in 2nd Mode of Data 2.

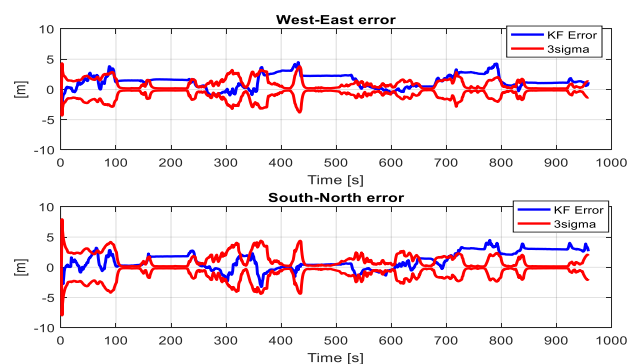


Figure 18. Estimated Horizontal Error in 3rd Mode of Data 2.

6 CONCLUSIONS AND FUTURE WORK

6.1 Conclusions

This study develops an integrated INS/GNSS (GPS+GLONASS) study for land vehicle applications, using carrier phase measurement for high accuracy. Conclusions are taken from 2 experimental data collect performed in light and deep urban environment in Toulouse.

The coupling of a low-cost single frequency receiver with low-cost IMU does not boost the positional accuracy when the GNSS signals are received in good condition. However, the improvement brought by low-cost IMU when operating in a constrained environment is put in evidence. With no carrier phases taken into account, meter-level performance is ensured in both urban environment.

When considering carrier phase measurements, the importance of CS-DR is stressed. The miss-detection and false-detection of CS both deteriorate the solution, by biasing the position at certain period of the data collect. The carrier phase measurements are probably not fully used due to difficulty to detect and repair reliably CSs in a difficult condition.

6.2 Future Work

The proposed work can be improved in following aspects:

1. For this study, only the GPS and GLONASS constellations are taken into account because the low-cost receiver does not currently process Galileo signals and the visibility of BeiDou satellites in Toulouse is rare. We believe that the inclusion of Galileo and BeiDou constellations would bring more reliability on PVT solutions.
2. Our proposed CS-DR relies too much on the satellite geometry quality. CS-free satellite can not continue to be used when the number of CS-free satellites is less than 4. CS-free satellite should be better tackled in the future.
3. Efforts to fix the carrier-phase integer ambiguities should made in following works.

7 REFERENCES

- [1] Priyanka Aggarwal. 2010. *MEMS-based integrated navigation*. Artech House.
- [2] John Egyir Aggrey. 2014. Multi-GNSS Precise Point Positioning Software Architecture and Analysis of GLONASS Pseudorange Biases. York University Toronto.
- [3] Antonio Angrisano. 2010. GNSS/INS integration methods.
- [4] Philippe Brocard. 2016. Integrity monitoring for mobile users in urban environment.
- [5] Robert Grover Brown and Patrick Y. C. Hwang. 2012. *Introduction to random signals and applied Kalman filtering: with MATLAB exercises* (4. ed ed.). Wiley, Hoboken, NJ.
- [6] S. Carcanague. 2013. Low cost GPS GLONASS Precise Positioning Algorithm in Constrained Environment. Institut National Polytechnique de Toulouse.
- [7] Jumping Chen, Pei Xiao, Yize Zhang, and Bin Wu. 2013. GPS/GLONASS System Bias Estimation and Application in GPS/GLONASS Combined Positioning. In *China Satellite Navigation Conference (CSNC) 2013 Proceedings*, Jiadong Sun, Wenhai Jiao, Haitao Wu and Chuang Shi (eds.). Springer Berlin Heidelberg, Berlin, Heidelberg, 323–333.
- [8] Shi Chuang, Yi Wenting, Song Weiwei, Lou Yidong, Yao yibin, and Zhang Rui. 2013. GLONASS pseudorange inter-channel biases and their effects on combined GPS/GLONASS precise point positioning. *GPS Solut.* 17, 4 (October 2013), 439–451.
- [9] IEEE Computer Society LAN MAN Standards Committee, International Organization for Standardization, and International Electrotechnical Commission. 1998. *IEEE standard specification format guide and test procedure for single-axis interferometric fiber optic gyros*. Institute of Electrical & Electronics Engineers (IEEE).
- [10] Naser El-Sheimy, Haiying Hou, and Xiaoji Niu. 2008. Analysis and Modeling of Inertial Sensors Using Allan Variance. *IEEE Trans. Instrum. Meas.* 57, 1 (January 2008), 140–149.
- [11] Anne-Christine Escher. 2003. Study of the Contribution of GNSS/INS Hybridization to GNSS Integrity Monitoring for Civil Aviation Applications.
- [12] Jianghui Geng, Qile Zhao, Chuang Shi, and Jingnan Liu. 2017. A review on the inter-frequency biases of GLONASS carrier-phase data. *J. Geod.* 91, 3 (March 2017), 329–340.
- [13] Saurabh Godha. 2006. Performance evaluation of low cost MEMS-based IMU integrated with GPS for land vehicle navigation application. Library and Archives Canada.
- [14] Paul D. Groves. 2013. *Principles of GNSS, Inertial, and Multisensor Integrated Navigation Systems*. Artech House.
- [15] H. Yamada, T. Takasu, N. Kubo, and A. Yasuda. 2010. Evaluation and Calibration of Receiver Inter-channel Biases for RTK-GPS/GLONASS.
- [16] Heidi Kuusniemi and Gérard Lachapelle. 2004. GNSS signal reliability testing in urban and indoor environments. In *Proceedings of the NTM Conference*.
- [17] Dmitry Kozlov, Michael Tkachenko, and Andrei Tochilin. 2000. Statistical characterization of hardware biases in GPS+ GLONASS receivers.
- [18] Sameh Nassar, Klaus-Peter Schwarz, Naser EL-Sheimy, and Aboelmagd Noureldin. 2004. Modeling inertial sensor errors using autoregressive (AR) models. *Navigation* 51, 4 (2004), 259–268.
- [19] Aboelmagd Noureldin, Tashfeen B. Karamat, and Jacques Georgy. 2013. *Fundamentals of Inertial Navigation, Satellite-based Positioning and their Integration*. Springer Berlin Heidelberg, Berlin, Heidelberg.
- [20] Robert Odolinski, Peter J. G. Teunissen, and Dennis Odijk. 2015. Combined BDS, Galileo, QZSS and GPS single-frequency RTK. *GPS Solut.* 19, 1 (January 2015), 151–163. DOI: <https://doi.org/10.1007/s10291-014-0376-6>
- [21] Mark G. Petovello. 2004. Real-time integration of a tactical-grade IMU and GPS for high-accuracy positioning and navigation.
- [22] Alex Quinchia, Gianluca Falco, Emanuela Falletti, Fabio Dovia, and Carles Ferrer. 2013. A Comparison between Different Error Modeling of MEMS Applied to GPS/INS Integrated Systems. *Sensors* 13, 8 (July 2013), 9549–9588.
- [23] Eun-Hwan Shin. 2005. Estimation Techniques for Low-Cost Inertial Navigation. The University of Calgary.
- [24] Sandra Verhagen, Christian Tiberius, Bofeng Li, and Peter JG Teunissen. 2012. Challenges in ambiguity resolution: biases, weak models, and dimensional curse. In *Satellite Navigation Technologies and European Workshop on GNSS Signals and Signal Processing, (NAVITEC), 2012 6th ESA Workshop on*, 1–8.
- [25] Lambert Wanninger. 2012. Carrier-phase inter-frequency biases of GLONASS receivers. *J. Geod.* 86, 2 (February 2012), 139–148.
- [26] Lambert Wanninger and S Wallstab-Freitag. 2007. Combined Processing of GPS, GLONASS, and SBAS Code Phase and Carrier Phase Measurements.
- [27] Oliver J. Woodman. 2007. *An introduction to inertial navigation*. University of Cambridge, Computer Laboratory.
- [28] Xsens Technologies. 2010. *MTi and MTx User Manual and Technical Documentation - Version O*.

ANNEX

In Eq.(12), detailed representations of mentioned term are:

- $\mathbf{r}_{nb}^n = (\varphi, \lambda, h)^T$ the geodetic coordinates of the moving object (herein, center of IMU);
- $\mathbf{v}_{nb}^n = (v_e, v_n, v_u)^T$ is the velocity vector in n -frame, consisting of east, north, up, three components;
- \mathbf{F}_{rv} is a transformation matrix describing the relationship between the derivative of geodetic coordinates and the velocity:

$$\mathbf{F}_{rv} = \begin{bmatrix} 0 & \frac{1}{R_M + h} & 0 \\ \frac{1}{(R_N + h)\cos\varphi} & 0 & 0 \\ 0 & 0 & 1 \end{bmatrix}$$

With $R_N = \frac{a}{\sqrt{1-e^2\sin^2\varphi}}$ is the normal radius, $R_M = \frac{a(1-e^2)}{\sqrt{(1-e^2\sin^2\varphi)^3}}$ the meridian radius.

- \mathbf{f}_{ib}^b is the specific force measurements (corrected) under b -frame
- $\boldsymbol{\Omega}_{ie}^n = [\mathbf{w}_{ie}^n \times]$, with $\mathbf{w}_{ie}^n = \begin{bmatrix} 0 \\ w_{ie}\cos\varphi \\ w_{ie}\sin\varphi \end{bmatrix}$ the notation of the Earth rotation rate vector under n -frame
- $\boldsymbol{\Omega}_{en}^n = [\mathbf{w}_{en}^n \times]$, with the angular velocity of the n -frame w.r.t the e -frame expressed in n -frame

$$\mathbf{w}_{en}^n = \begin{bmatrix} -\dot{\varphi} \\ \dot{\lambda}\cos\varphi \\ \dot{\lambda}\sin\varphi \end{bmatrix} = \begin{bmatrix} \frac{-v_n}{R_M + h} \\ \frac{v_e}{R_N + h} \\ \frac{v_e \tan\varphi}{R_N + h} \end{bmatrix}$$

- $\mathbf{g}^n = \begin{bmatrix} 0 \\ 0 \\ -g \end{bmatrix}$ is the Earth's gravity field.

- $\mathbf{F}_{rr} = \begin{bmatrix} 0 & 0 & \frac{-v_n}{(R_M+h)^2} \\ \frac{\sin\varphi \cdot v_e}{(R_N+h)\cos^2\varphi} & 0 & \frac{-v_e}{(R_N+h)^2\cos\varphi} \\ 0 & 0 & 1 \end{bmatrix}$
- $\mathbf{F}_{rv} = \begin{bmatrix} 0 & \frac{1}{R_M+h} & 0 \\ \frac{1}{(R_N+h)\cos\varphi} & 0 & 0 \\ 0 & 0 & 1 \end{bmatrix}$
- $\mathbf{F}_{vr} = \begin{bmatrix} 2w_{ie}v_u\sin\varphi + 2w_{ie}v_n\cos\varphi + \frac{v_e v_n}{(R_N+h)\cos^2\varphi} & 0 & \frac{v_e v_u}{(R_N+h)^2} - \frac{v_e v_n \sin\varphi}{(R_N+h)^2 \cos\varphi} \\ -2w_{ie}v_e\cos\varphi - \frac{v_e^2}{(R_N+h)\cos^2\varphi} & 0 & \frac{v_n v_u}{(R_M+h)^2} + \frac{v_e^2 \sin\varphi}{(R_N+h)^2 \cos\varphi} \\ -2w_{ie}v_e\sin\varphi & 0 & \frac{-v_n^2}{(R_M+h)^2} + \frac{-v_e^2}{(R_N+h)^2} + \frac{2g}{R+h} \delta h \end{bmatrix}$
- $\mathbf{F}_{vv} = \begin{bmatrix} \frac{-v_u}{(R_N+h)} + \frac{v_n \sin\varphi}{(R_N+h)\cos\varphi} & 2w_{ie}\sin\varphi + \frac{v_e \sin\varphi}{(R_N+h)\cos\varphi} & -2w_{ie}\cos\varphi - \frac{v_e}{(R_N+h)} \\ -2w_{ie}\sin\varphi - \frac{2v_e \sin\varphi}{(R_N+h)\cos\varphi} & \frac{-v_u}{(R_M+h)} & \frac{-v_n}{(R_M+h)} \\ \frac{2v_e}{(R_N+h)} + 2w_{ie}\cos\varphi & \frac{2v_n}{(R_M+h)} & 0 \end{bmatrix}$
- $\mathbf{F}_{ee} = -\boldsymbol{\Omega}_{in}^n = -[(\mathbf{w}_{ie}^n + \mathbf{w}_{en}^n) \times] = \begin{bmatrix} 0 & w_{ie}\sin\varphi + \frac{v_e \tan\varphi}{(R_N+h)} & -w_{ie}\cos\varphi - \frac{v_e}{R_N+h} \\ -w_{ie}\sin\varphi - \frac{v_e \tan\varphi}{(R_N+h)} & 0 & \frac{-v_n}{R_M+h} \\ w_{ie}\cos\varphi + \frac{v_e}{R_N+h} & \frac{v_n}{R_M+h} & 0 \end{bmatrix}$
- $\boldsymbol{\Omega}_{nb}^b = [\mathbf{w}_{nb}^b \times] = [\mathbf{w}_{ib}^b \times] + [\mathbf{w}_{ne}^b \times] + [\mathbf{w}_{ei}^b \times] = [\mathbf{w}_{ib}^b \times] - \mathbf{C}_n^b [\mathbf{w}_{en}^n \times] \mathbf{C}_n^b - \mathbf{C}_n^b [\mathbf{w}_{ie}^n \times] \mathbf{C}_n^b$, the skew-symmetric of the Earth rotation rate under b -frame;
- $\mathbf{F}_{ve} = [\mathbf{C}_b^n \mathbf{f}_{ib}^b \wedge] = \begin{bmatrix} 0 & -f_u & f_n \\ f_u & 0 & -f_e \\ -f_n & f_e & 0 \end{bmatrix}$
- $\mathbf{F}_{er} = \begin{bmatrix} 0 & 0 & \frac{v_n}{(R_M+h)^2} \\ -w_{ie}\sin\varphi & 0 & -\frac{v_e}{(R_N+h)^2} \\ w_{ie}\cos\varphi + \frac{v_e}{(R_N+h)\cos^2\varphi} & 0 & -\frac{v_e \tan\varphi}{(R_N+h)^2} \end{bmatrix}$
- $\mathbf{F}_{ev} = \begin{bmatrix} 0 & \frac{-1}{(R_M+h)} & 0 \\ \frac{1}{R_N+h} & 0 & 0 \\ \frac{\tan\varphi}{(R_N+h)} & 0 & 0 \end{bmatrix}$

In Eq.(12) where INS error state dynamics are showed, detailed representations of those compact terms are: